



3D printing PEDOT-CMC-based high areal capacity electrodes for Li-ion batteries

Pengqiang Bao¹ · Ying Lu¹ · Pan Tao¹ · Bailin Liu² · Jinlian Li¹ · Xiaoling Cui¹

Received: 19 March 2021 / Revised: 9 April 2021 / Accepted: 14 April 2021 / Published online: 20 April 2021
© The Author(s), under exclusive licence to Springer-Verlag GmbH Germany, part of Springer Nature 2021

Abstract

Lithium-ion micro-batteries (LIMBs) with higher energy density have drawn extensive attention. 3D printing technique based on direct ink writing (DIW) is a low-cost and simple approach to fabricate LIMBs especially with higher areal capacity. Herein, poly(3,4-ethylenedioxythiophene):polystyrene sulfonate (PEDOT:PSS) nanofibrils are first combined with carbon methyl cellulose (CMC) to achieve the 3D printing of thick LFP (LiFePO₄)-PEDOT-CMC electrodes at room temperature by DIW. 3D-printed PEDOT-CMC-based composite thick electrodes demonstrate high conductivity because of the interconnected 3D network including hierarchical macro-micro porous criss-crossing filaments which can provide effective transport paths for Li ions and electrons. Further, LFP-PEDOT-CMC electrodes of different thicknesses are 3D-printed to study the effect of thicknesses on the electrochemical performances. The 3D-printed ultra-thick LFP-CMC-PEDOT electrode of 1.43 mm thickness at lower rate exhibits a highly improved areal capacity (5.63 mAh cm⁻², 0.2 C) and high capacity retention (after 100 cycles, 0.2 C, 92%). The rate capability decreases steadily with the increasing thickness. However, for the extra-thick electrodes greater than 1.43 mm thickness, the discharge capacity, rate, and cycle capability decline dramatically. Electrochemical impedance spectroscopy measurements are used to explain the kinetic mechanism. For 3D-printed LFP-CMC-PEDOT electrodes blow 1.43 mm thickness, the 3D network plays the dominant role to maintain the effective transmission dynamics regardless of electrode thickness. But for the extra-thick electrodes, the greater transport distance becomes the major limiting factor resulting in the degradation of electrochemical performances. This work will offer guidance on how to apply 3D-printed ultra-thick electrodes with high energy density to LIMBs.

Keywords PEDOT · 3D printing · Thick electrodes · Li-ion battery · Areal capacity

Introduction

Recent advancements in lithium-ion batteries (LIBs) are moving toward miniaturization to meet the developing requirements of smart portable, wearable, and integrated electronics [1–4]. Compared with bulky batteries, lithium-ion micro-batteries (LIMBs) with higher energy density, better mechanical flexibility, lighter weight, and higher thermodynamic stability have become a major research focus [5–8]. Coating the

electrode materials onto the current collector is the traditional fabrication process for LIBs. There are many weaknesses about this approach leading to poor charge storage performance, such as inhomogeneous mixing and coating, loose contact, and easy delamination from the collector. In fact, the low mass loading of these thin electrodes, usually below 1 mg cm⁻², is the chief intrinsic drawback of this approach. Most attempts to mitigate these issues have concentrated on introducing doping additives [9], constructing hierarchically porous nano-micro structure [10] and regulating the ratio of activity materials, conductive additives, and adhesives [11]. But it is so difficult for these strategies to overcome the critical shortcoming of fixed shapes, bulky volume, and heavy weight that they are hardly applied to LIMBs. Another limitation of conventional flat electrodes fabricated by coating approach is that the capacity will degrade simply by increasing the thickness and mass loading (over 10 mg cm⁻²) because of the mass transport hindrance for ions and electrons [12].

✉ Xiaoling Cui
xlculw@163.com

¹ College of Petrochemical Technology, Lanzhou University of Technology, 36 Pengjiaping Road, Lanzhou 730050, Gansu Province, China

² School of Mechanical and Electrical Engineering, Lanzhou University of Technology, Lanzhou 730050, China

3D printing, birthed by CAD on a computer, provides an opportunity to form fixed structures with ease, especially for appropriate products with minimal gravimetric and volumetric footprints [13]. 3D printing method has been classified into seven categories [14] including material extrusion (ME), binder jetting (BJ), material jetting (MJ), powder bed fusion (PBF), VAT photopolymerization (VAT-P), sheet lamination, and direct energy deposition (DED). For LIBs, most of the work has been focused on material extrusion and jetting-based methods. Direct ink writing (DIW) has become the most widely used 3D printing extrusion method for LIBs as the viscoelastic ink can be directly extrude from the nozzle to fabricate layer-by-layer architectures in accordance with the computer designed pattern [15]. Because the DIW technique has the advantages of affordable price, easy operation, and high resolution, it has been used to print all components in the battery. For example, Sun et al. fabricated the first interdigitated LIMBs via DIW [16]. In their works, highly concentrated LiFePO_4 (LFP) and $\text{Li}_4\text{Ti}_5\text{O}_{12}$ (LTO) nanoparticles were dispersed into the complex aqueous systems containing glycerol, ethylene glycol, and cellulose-based viscosifiers to constitute 3D printing ink with good rheological properties. This 3D-printed micro-battery yielded an areal capacity of 1.2 mAh cm^{-2} at 0.5 C . They further studied the effect of different electrode thicknesses on the areal energy and the power density by 3D printing customized LIBs, demonstrating that the 1-mm-thick packaging battery delivered an areal capacity of 4.45 mAh cm^{-2} at a current density of 0.14 mA cm^{-2} [17].

On the other hand, cellulose can act as binder and surfactant to endow 3D-printed ink with unique viscoelastic performance owing to its rich hydroxyl groups [18–20]. But cellulose-based 3D-printed materials face obstacles that cellulose thermally decomposes and becomes flowable when heated. Apart from that, adding too much cellulose will sacrifice the conductivity of the whole batteries. Thus, it is difficult to construct cellulose-based 3D-printed ink for LIBs at room temperature. Liu et al. explored a low temperature direct writing technique (LTDW) by adding 1,4-dioxane as a freezing agent to carbon methyl cellulose (CMC) and fabricated LTO ultra-thick porous electrodes with high mass loading [21]. But these thick LTO electrodes still depended on the foam copper as substrate to maintain the properties of high ductility and specific surface area. How to use the cellulose-based viscosifiers to fabricate the free-standing thick electrode at room temperature and achieve the effective ion and electron transmission simultaneously in LIBs is a key challenge to face.

Poly(3,4-ethylenedioxythiophene):poly(styrenesulfonate) (PEDOT:PSS) has attracted great attention based on its high conductivity, high stability, biocompatibility, and solution processability [22–24]. Many researches in LIBs showed that adding or coating PEDOT:PSS into the electrodes could effectively improve the electrical conductivity by forming a

more homogeneous electrode sheet and thus had more favorable electrochemical kinetics [25–27]. Zhao et al. developed a favorable rheological 3D-printable conducting polymer ink based on PEDOT:PSS. Because of the superior printability, high resolution, and high aspect ratio microstructure, PEDOT-based conducting polymers were 3D-printed and converted into various conducting polymer devices [28].

In this work, we first introduced PEDOT:PSS to accomplish 3D printing porous thick cellulose-based electrodes with high mass loading of LFP. Under the synergic effect of PEDOT:PSS and CMC, these viscoelastic inks were directly 3D-printed into programmed free-standing 3D structures just in air at room temperature by DIW. The cooperated mechanisms of PEDOT:PSS and CMC were put forward to explain the reason why they can effectively improve the printability and conductivity properties of electrodes. In addition, to study the effect of thicknesses on the electrochemical performance, LFP-CMC-PEDOT electrodes with different thicknesses were 3D-printed. Eight-layer LFP-CMC-PEDOT cathode with the thickness of 1.43 mm achieved high mass loading of 39.9 mg cm^{-2} and showed improved areal capacity of $\sim 5.63 \text{ mAh cm}^{-2}$ at 0.2 C . It also exhibited high recycling performance with a capacity retention of 92% after 100 cycles at 0.2 C . These results surpassed those of conventional coating electrodes. This study provides a new strategy that viscoelastic conducting polymers replacing other conductivity-free viscosifiers can be directly applied to 3D printing design to achieve faster ion and electron transfer and higher energy and power density in LIMBs.

Experimental section

Materials and methods

LiFePO_4 (LFP) nanoparticles (150 nm) and Super P (SP) were acquired from Guangdong Canrd New Energy Technology Co., Ltd. Carbon methyl cellulose (CMC, $M_w=250,000$) was purchased from Shanghai Macklin Biochemical Co., Ltd. Poly(3,4-ethylenedioxythiophene):poly(styrenesulfonate) (PEDOT:PSS) aqueous solution (1.5 wt%) was obtained from Orgacon DRY, Belgium.

Preparation of 3D-printable inks

A 3D-printed ink consists of LFP nanoparticles, conductive agents (Super P, SP), and binders (CMC and PEDOT). CMC was dissolved in the deionized water to a viscous solution with 5 wt%. PEDOT:PSS nanofibrils were prepared by cryogenically frozen and lyophilized method [28] from a commercially available aqueous solution. The fully grinding LFP and SP mixtures were added into 5 wt% CMC and grinded again. Then the as-prepared PEDOT:PSS nanofibrils were dispersed

into these mixtures to obtain a homogeneous ink. The mass ratio of CMC and PEDOT:PSS was 1:1. The LFP mass loading was 15 g/40 mL. The viscoelastic ink consists of 80.0 wt% LFP, 10.0 wt% SP, 5.0 wt% CMC, and 5.0 wt% PEDOT:PSS in deionized water.

3D printing LFP and LTO electrodes

3D printer (JD200mini) was applied to print electrodes layer by layer using a preprogrammed patterning procedure. Inks were printed from the nozzle of 250 μm at a moving speed of 120 mm min^{-1} according to the designed square stacking framework (1 $\text{mm} \times 1 \text{mm}$) with various layers in which the center-to-center rod space was 500 μm and the rod diameter was 250 μm . The integrated air-powered fluid dispenser was used to control the ink flow with a nozzle pressure of 2 bars. Electrodes with different thicknesses were printed onto a glass slide and frozen in a refrigerator under $-20 \text{ }^\circ\text{C}$ for 12 h. And then water in the electrodes was removed by a freeze-drying process for 48 h. 3D printing electrodes were vacuum dried at 100 $^\circ\text{C}$ for 8 h to keep dry thoroughly.

Characterizations

The rheological behavior of the inks was conducted by an Anton Paar MCR92 rheometer with a 20-mm-diameter steel parallel-plate geometry at room temperature ($\sim 25 \text{ }^\circ\text{C}$). The shear viscosity of inks was measured by a steady-state flow step test at shear rates from 0.1 to 1000 s^{-1} . Shear storage modulus (G') and loss modulus (G'') were performed as a function of shear stress at an oscillation stress of 1–1000 Pa at 1 Hz shear.

A scanning electron microscopy (SEM, JSM-5600, Japan) was used to observe the morphology. The conductivity of 3D-printed electrode was measured by a four-point probe measurement. During the test, the contact points of four probes are placed on the flat and smooth surface of electrode sheets with different thicknesses, including the two ends and 1/3 and 2/3 of the middle, respectively. The conductivity was calculated according to the I-V curves.

The 3D-printed LFP electrodes were directly used as cathodes to be assembled into CR2032 coin cells using lithium foil as the anode. 1 mol L^{-1} lithium hexafluorophosphate (LiPF_6) in the mixed solvent of ethylene carbonate (EC) and diethyl carbonate (DEC) (1:1, V: V) was selected as the electrolyte. Electrochemical charge and discharge tests were performed on a LAND CT2001A tester (Wuhan, China) (2.0 V \sim 4.0 V, vs Li^+/Li , for LFP-CMC-PEDOT) at 25 $^\circ\text{C}$. The electrochemical impedance spectroscopy (EIS) analysis on CHI660C electrochemical analyzer with three-electrode system (Shanghai, China) was measured at the fully delithiated state of 4.0 V (for LFP-CMC-PEDOT) between 100 kHz and 10 MHz with 5 mV amplitude.

Results and discussion

Rheological measurements of different inks were performed to explain why LFP-CMC-PEDOT show the better printability compared with LFP-CMC (Fig. 1). As shown in Fig. 1a, the viscosities almost decrease linearly with increasing shear rates. On the other hand, Fig. 1b shows that the value of the storage modulus (G') is noticeably higher than that of the loss modulus (G'') under the oscillation strain up to 55 and 100, exhibiting solid-like behavior. When the oscillation strain continues to rise, $G'' > G'$, indicating that viscous deformation begins to take the dominant property. Thus, both inks exhibit similar shear-thinning behavior, confirming that they are non-Newtonian fluids and can be printed [29]. But in Fig. 1a, LFP-CMC ink has an apparent viscosity of $10^2 \text{ Pa}\cdot\text{s}$ at a shear rate of 1 s^{-1} , while LFP-CMC-PEDOT has the one ranging from 10^3 to $10^4 \text{ Pa}\cdot\text{s}$, one order of magnitude higher. More steep decrease in viscosity with shear rate and much higher viscosity enable LFP-CMC-PEDOT ink much easier to be 3D-printed as complex 3D structures and design patterns at room temperature. In addition, in Fig. 1b, the flex point of $G'' > G'$ of LFP-CMC-PEDOT locates at greater strain in comparison with LFP-CMC-PEDOT. The longer storage modulus plateau and the higher moduli value are essential for 3D printing stacked architectures. As a consequence, PEDOT plays a significant role in improving the printability under mild conditions for CMC-based LFP ink.

Figure 2 compares the height/thickness as a function of layer numbers of both inks. LFP-CMC and LFP-CMC-PEDOT ink were prepared to be printed on glass with 2, 4, 8, 10, and 12 layers at room temperature. But as shown in illustration, for LFP-CMC inks with multi-layer, the shape and geometry are hard to maintain and the filament adheres and overlaps. When adding PEDOT, thicknesses in different 3D-printed LFP-CMC-PEDOT electrodes have a linear relationship with layer numbers. The thicknesses for 2-, 4-, 8-, 10-, and 12-layer LFP-CMC-PEDOT electrodes are 0.396, 0.808, 1.429, 1.742, and 2.088 mm, respectively. The average thickness of one layer was $\sim 0.20 \text{ mm}$. The lower layer especially the ground layer demonstrates exceptional shape retention, which is contributed to the synergistic viscoelastic properties of both CMC and PEDOT.

To analyze the architecture of the electrodes, SEM images of LFP-CMC-PEDOT and LFP-CMC electrodes were taken in Fig. 3. The hierarchical criss-cross 3D architecture of 8-layer LFP-CMC-PEDOT is observed in Fig. 3a from the top down. Continuous filaments were constructed with diameter (D) $\sim 200 \text{ } \mu\text{m}$ and the space interval (L) between two filaments $\sim 250 \text{ } \mu\text{m}$. Two layers next to each other arrange in a criss-cross pattern. Every 3D-printed LFP-CMC-PEDOT filament is self-standing layer by layer to form macropores at the intersection. Each layer arrays neatly and shows low tortuosity. Thus macropores with low tortuosity are connected

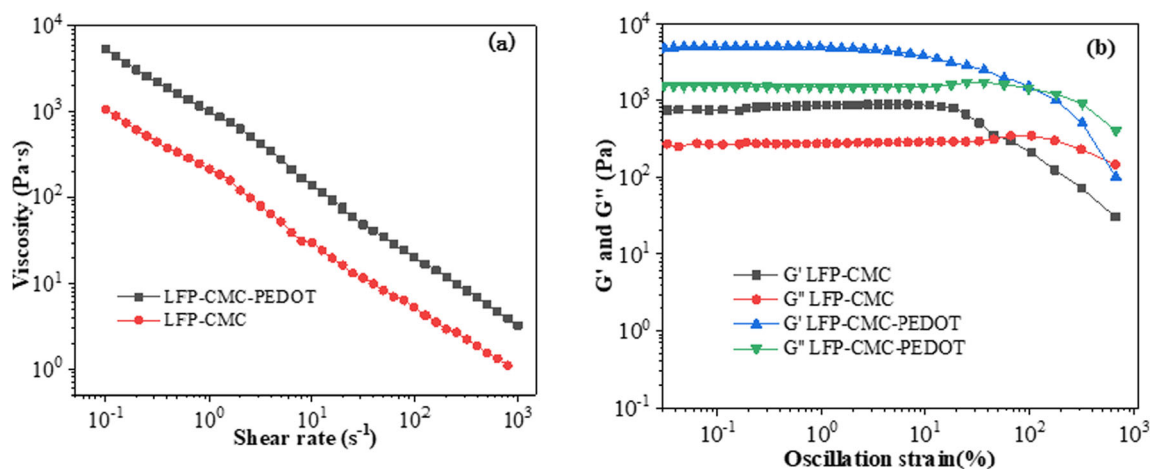


Fig. 1 Rheological properties of the LFP-CMC ink and LFP-CMC-PEDOT composite ink: (a) apparent viscosity, (b) storage modulus (G'), and loss modulus (G'')

vertically. Furthermore, due to freeze-drying, the surface of each filament is covered with additional micrometer-sized pore. Figure 3 b shows the 3D-crosslinked pores magnified of the red zone in one LFP-CMC-PEDOT filament. The aperture of the micrometer-sized pores ranges from several to tens of microns. However, in Fig. 3c, LFP-CMC electrode shows irregular pore. Only scattered pores with a few microns can be seen. Most pores are wrapped by the aggregation of CMC and SP carbon particles [21]. So LFP-CMC electrodes are proved hard to provide transmission channel for ions and electrons, while LFP-CMC-PEDOT electrodes with the hierarchical 3D architecture, constructed with 250 μm wide square pores between the filaments combining micrometer-sized pores in every filament, can not only facilitate the penetration of the liquid electrolyte [30] but also act as a chamber to store the electrolyte [31]. In addition, the 3D network of LFP-CMC-PEDOT electrodes benefits the transmission of electrons even in thick electrodes and demonstrates good

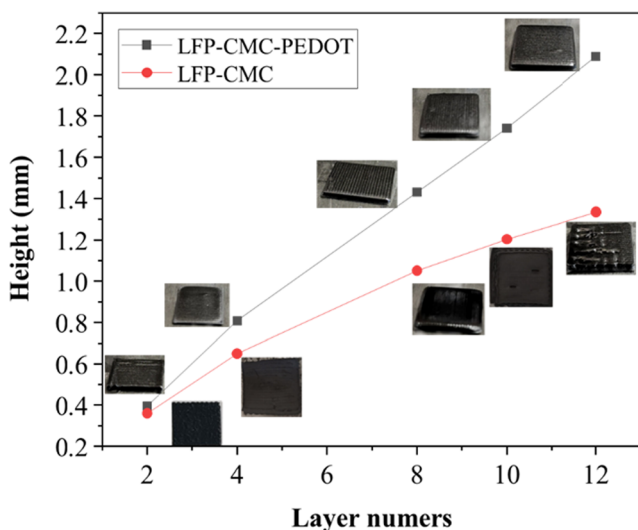


Fig. 2 Heights of 3D-printed electrodes as a function of layer number

conductivity. The electrical conductivities of 8-layer LFP-CMC-PEDOT and LFP-CMC electrodes tested using four-probe method are 10.3 S cm^{-1} and 0.9 S cm^{-1} , respectively, which further proves that PEDOT can effectively improve electrical conductivity.

Figure 4 exhibits the 3D printing process of PEDOT-CMC-based gelation electrodes. It explains the synergistic effect of PEDOT, and CMC contributes to the improvement of conductivity and printability for LFP electrodes.

It is known to all that PEDOT:PSS suspension in water has a core-shell structure, in which hydrophilic PSS⁻ shell surrounds the hydrophobic PEDOT⁺ [32] (Fig. 4a). Entangled PEDOT-PSS nanofibrils are obtained by lyophilization in a cryogenic condition from dilute dispersion of PEDOT-PSS [28] (Fig. 4b). On one hand, this process increases the π - π stacking and the crystallinity of PEDOT, which is beneficial to the conductivity of PEDOT-PSS. On the other hand, the formation of reversible physical networks endows PEDOT-PSS nanofibrils better viscoelasticity so that PEDOT-PSS nanofibrils can be 3D-printed. Further, once adding PEDOT-PSS nanofibrils to CMC, CMC acts as an acidic surfactant and provides sufficient H⁺ to protonate the PSS⁻. The electrostatic attraction between PEDOT⁺ and PSS⁻ chains gradually decreases. PEDOT⁺ chains are subsequently exposed to each other. Due to π - π stacking and hydrophobic attractions, a connected 3D network with higher viscoelasticity and conductivity is formed (Fig 4c). Taking advantage of its high viscosity, LFP and SP nanoparticles are stick tightly and homogeneously dispersed into this 3D network (Fig. 4d). Thus, the hierarchical 3D architecture can be 3D-printed into self-standing structures with various shapes and facilitate the transfer and transmission of Li ions and electrons in the charging and discharging process (Fig. 4e).

All 3D-printed LFP-CMC-PEDOT electrodes were assembled into coin cells to evaluate the effect of different thicknesses (2, 4, 8, 10, and 12 layers) on the electrochemical

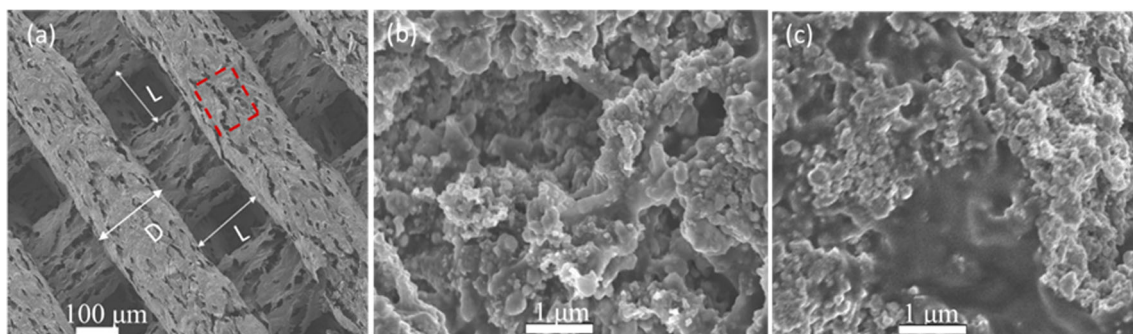


Fig. 3 (a) Top-down SEM image of the LFP-CMC-PEDOT electrode, (b) magnified SEM image of the red zone in a LFP-CMC-PEDOT filament, and (c) SEM image of the LFP-CMC electrode

performances. The 2nd charge/discharge curves of LFP-CMC-PEDOT electrodes with variable thickness at 0.2 C are shown in Fig. 5. Figure 5a shows that the charge/discharge curves for the 2-, 4-, and 8-layer electrodes remain longer flat plateaus of 3.4 V, which are the typical discharge behavior of olivine LFP. These electrodes deliver a discharge capacity of 155.9, 147.0, and 141.2 mAh g⁻¹, respectively. Compared with the convention coated LFP electrodes containing PEDOT/CMC binder, these 3D-printed thicker electrodes show slightly higher specific capacity [26, 33]. In contrast, the potential plateaus of the 10-layer and the 12-layer electrode become shorter, and the discharge capacities are only 128.4 and 109.7 mAh g⁻¹, respectively. This behavior indicates that 3D-printed LFP-CMC-PEDOT electrodes have a lower polarization at low charge/discharge rate. With the increase of thickness, the polarization becomes larger. Figure 5b further shows the areal capacities of different layer-LFP-CMC-PEDOT electrodes at 0.2 C. The area capacity gradually increases with increasing electrode thickness.

But due to the shorter voltage platform of 10 layers and 12 layers, the increasing rate degrades rapidly, while 8-layer LFP-CMC-PEDOT electrode keeps increasing steadily, showing an impressive areal capacity of 5.63 mAh cm⁻² (1.43 mm, active mass loading 39.9 mg).

Figure 6 shows the rate capacities of LFP-CMC-PEDOT electrodes of different thicknesses at charge/discharge rates from 0.2 C to 5 C. These results reach the similar conclusion that good kinetics of 3D-printed LFP-CMC-PEDOT electrodes with smaller thickness can be obtained at lower rates. Note that the capacity of 8-layer LFP-CMC-PEDOT at 2 C is about 100 mAh g⁻¹, in which the corresponding areal capacity is 3.5 mAh cm⁻². Even at 5 C, the value stays 2.7 mAh cm⁻². With the rate increasing from 2 C to 5 C, the distinct degradation of capacities is observed due to the slow kinetics of Li ions and electrons transport for 3D-printed thicker electrodes. Especially for the 10- and 12-layer electrodes, the capacity falls drastically below 20 mAh g⁻¹ at 5 C. These results predict that the 3D-printed porous electrodes with suitable

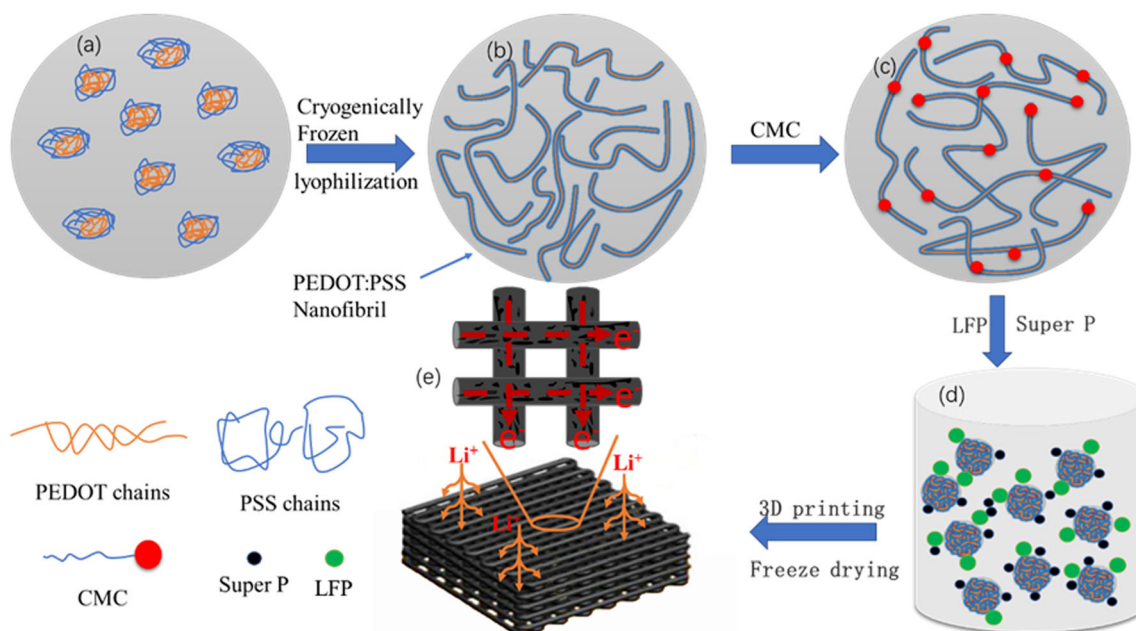
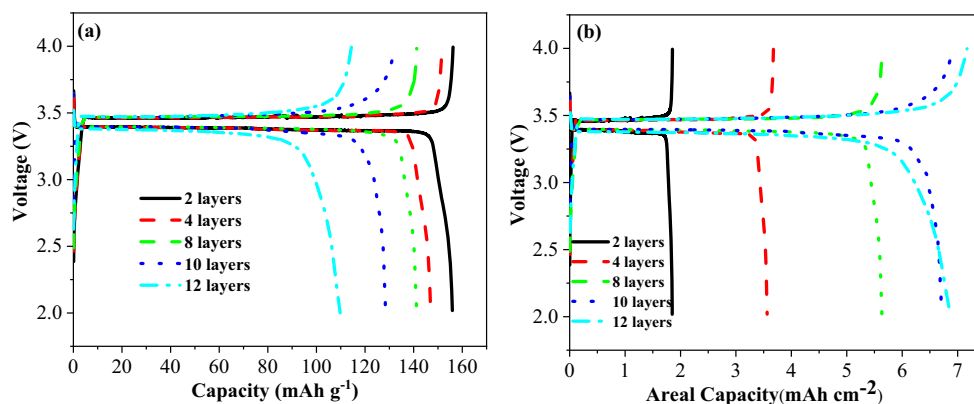


Fig. 4 Schematic illustration of the fabrication and 3D printing process of PEDOT-CMC-based gelation LFP-PEDOT-CMC electrodes

Fig. 5 The 2nd charge/discharge curves of 3D-printed LFP-CMC-PEDOT electrodes with different thicknesses at 0.2C: (a) capacity and (b) areal capacity



thickness can be applied to where the large amount of energy are required. How to improve the power density and rate capability of 3D-printed electrodes with the larger thickness is currently under investigation.

The cycle performances of the 3D-printed LFP-CMC-PEDOT electrodes at 0.2 C and 2 C-rate are illustrated in Fig. 7a and b, respectively. Table 1 gives the capacity retention of the electrodes at both rates. It can be observed that the capacity value at 0.2 C is retained at over 80% after 100 cycles for all of the printed electrodes. Higher capacity retention indicates that 3D-printed thick LFP-CMC-PEDOT electrodes can maintain the connected 3D network structure at a lower rate even if the thickness is more than 10 times the traditional coated electrodes. But when the rate increases to 2 C, the capacity retention decreases significantly especially for the extra-thick electrodes with 10 and 12 layers. Due to the longer transport distance of Li ions and electrons, it is difficult for them to provide a smooth path without tortuosity and void spaces, thereby leading to the degradation of capacities at the larger rate [21]. These cycle performance results are consistent with rate conclusions.

To explain the effect of different thicknesses on the transportation of ions and electrons in Li-ion cells, EIS was carried out over a frequency range from 10⁻² Hz to 10⁵ Hz. Nyquist plots of 3D-printed LFP-CMC-PEDOT electrodes of different thicknesses are illustrated in Fig. 8a. It can be seen that each of

the curve is composed of two parts: the semicircle at high frequencies and the oblique line at low frequencies. The equivalent circuit simulation shows that the spectrum from high to low frequency reflects the solution resistance R_{Ω} , the charge transfer resistance R_{ct} , and the Warburg impedance Z_w . Table 2 gives the values of fitted parameters. All the results of graphs and data show that the charge transfer resistance increases with increasing electrode thickness. These results are a further proof that the rate and cycle performance will degrade gradually with the increasing thickness. In addition, from 2 to 8 layers, the rate of the charge transfer resistance increases slowly. However, for the 10- and 12-layer LFP-CMC-PEDOT electrodes, the rate increase of resistance becomes rapid. The interconnected channels in 3D-printed electrodes of the thickness blow 1.43 mm can provide convenience for the infiltration of the electrolyte. Too much thickness is unfavorable for the transfer of electrons. The charge transfer resistance measurement gets the same conclusion as the result of the electrochemical test.

The Warburg impedance Z_w can reflect the process of Li-ion diffusion in the bulk of electrode. And the Li-ion diffusion coefficient can be calculated according to the following two equations [34]:

$$|Z'| = R_S + R_{ct} + \sigma_w \omega^{-0.5} D_{Li^+} = \frac{R^2 T^2}{2A^2 n^4 F^4 C_{Li}^2 \sigma^2}$$

Fig. 6 Rate performance comparison of 3D-printed LFP-CMC-PEDOT electrodes with different thicknesses: (a) rate capacity and (b) areal capacity

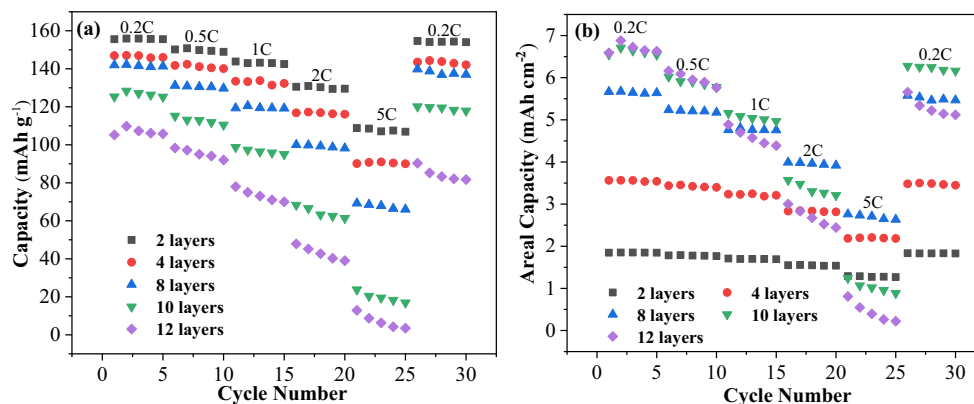


Table 1 Capacity retention (%) of the 3D-printed LFP-CMC-PEDOT electrodes of different thicknesses at different rates

Rate	2 layers	4 layers	8 layers	10 layers	12 layers
0.2 C	97%	95%	92%	87%	80%
2 C	92%	89%	84%	60%	30%

Figure 7b analyzes the linear relationship of Z' and $\omega^{-0.5}$. The slope of the curve is the value of σ_w . So the diffusion coefficient D_{Li^+} of 3D-printed LFP-CMC-PEDOT electrodes of different thicknesses are worked out and shown in Table 2, respectively. With the rising of electrode thickness, D_{Li^+} decreased. Compared with 10- and 12-layer LFP-CMC-PEDOT, D_{Li^+} of the 3D-printed electrodes with lower thicknesses is larger indicating Li-ion diffusion faster. The numerical results agree with those of available literatures [35, 36].

For the 3D-printed thick electrodes, the electrochemical performances root in the reaction kinetic of Li ions and electrons. 3D conductive network formed by the stacking composite PEDOT-CMC sticking LFP tightly contributes to the rapid transmission of electrons in interactive channels. The porous structure generated by filament spaces and abundant micropores facilitates the penetration of the electrolyte which is beneficial to the intercalation/deintercalation of Li ions. But for the extra-thick electrodes, the transport distance of Li ions become much larger. This will have a great adverse effect on the charge transfer and ion diffusion in the charging and discharging process. As a result, the 3D-printed LFP-CMC-PEDOT electrodes below 1.43 mm thickness show more increased electrochemical performance than conventional coated electrodes. Improving the dynamic behavior of 3D-printed electrodes with a greater thickness bring greater challenge for the future work.

Conclusion

In this work, new fabricated PEDOT:PSS nanofibrils were added into CMC to constitute composite viscoelastic ink to

Table 2 Impedance parameters of the 3D-printed LFP-CMC-PEDOT electrodes with different thicknesses

Samples	R_{Ω} (Ω)	R_{ct} (Ω)	D_{Li^+} ($cm^2 s^{-1}$)
2 layers	6.742	150.4	2.13×10^{-13}
4 layers	7.836	194.5	1.32×10^{-13}
8 layers	9.890	233.3	1.07×10^{-13}
10 layers	13.986	389.7	5.15×10^{-14}
12 layers	16.992	585.4	1.12×10^{-14}

stick LFP and Super P tightly. These LFP-PEDOT-CMC inks with high viscosity and printability can be 3D-printed as Li-ion cathodes by DIW at room temperature. Further, LFP-PEDOT-CMC electrodes with different thicknesses were 3D-printed to study the effect of thicknesses on the electrochemical performances. The 3D-printed ultra-thick LFP-CMC-PEDOT electrode of 1.43 mm thickness at lower rate exhibits a highly improved areal capacity (5.63 mAh cm^{-2} , 0.2 C) and high capacity retention (after 100 cycles, 0.2 C, 92%). The rate capability decreases steadily with the increasing thickness. However, for the extra-thick electrodes greater than 1.43 mm thickness, the discharge capacity, rate, and cycle capability decline dramatically. The morphology and EIS tests explore the kinetic mechanism. The results show that 3D-printed PEDOT-CMC-based composite electrodes demonstrate interconnected 3D network. Multiple criss-crossing filaments without tortuosity, wide square pores between the filaments combining micrometer-sized pores in every filament can provide effective transport paths for Li^+ and electrons which is beneficial to the penetration of the electrolyte and the charge transfer and transmission. But for the extra-thick electrodes, the transport distance are far so great that hinder the transmission dynamics. This work provides an avenue to accomplishing the application of 3D-printed electrodes with high capacity to LIMBs. Moreover, it brings out new challenges for researchers that mitigate the negative effect of 3D-printed ultra-thick electrodes.

Fig. 7 Cycle performance comparison of 3D-printed LFP-CMC-PEDOT electrodes with different thicknesses at different rates: (a) 0.2 C and (b) 2 C

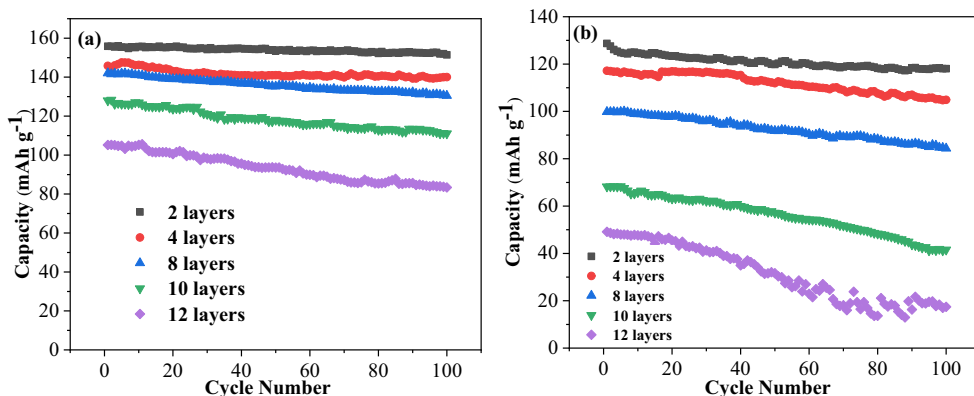
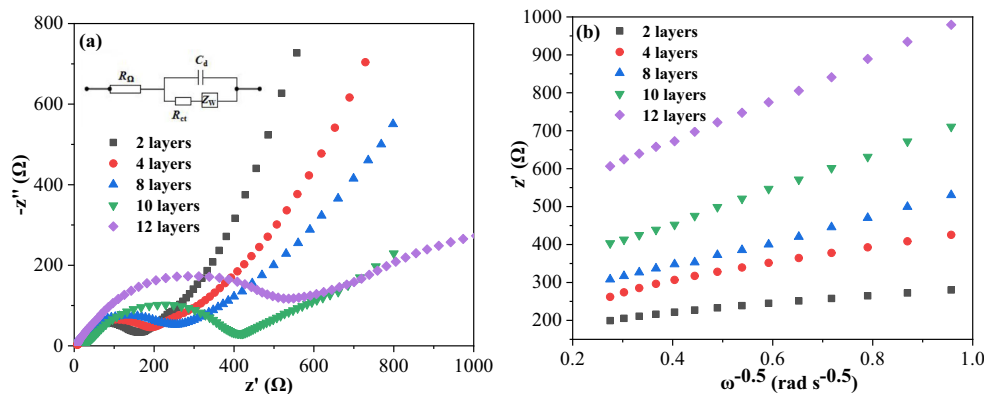


Fig. 8 Electrochemical impedance spectroscopy of cells for 3D-printed LFP-CMC-PEDOT electrodes with different thicknesses: (a) Nyquist plot and (b) Z' plotted against $\omega^{-0.5}$



Funding The work is supported by the National Undergraduate Innovation and Entrepreneurship Training Program in China (202010731020).

References

- Chen RS, Li QH, Yu XQ, Chen L, Li H (2020) Approaching practically accessible solid-state batteries: stability issues related to solid electrolytes and interfaces. *Chem Rev* 120:6820–6877
- Mackanic DG, Chang TH, Huang ZJ, Cui Y, Bao Z (2020) Stretchable electrochemical energy storage devices. *Chem Soc Rev* 49:4466–4495
- Chen D, Lou Z, Jiang K, Shen G (2018) Device configurations and future prospects of flexible/stretchable lithium-ion batteries. *Adv Funct Mater* 28:1805596
- Zubi G, Dufo-Lopez R, Carvalho M et al (2018) The lithium-ion battery: state of the art and future perspectives. *Renew Sust Energy* 89:292–308
- Nasreldin M, Delattre R, Calmes C, Ramuz M, Sugiawati VA, Maria S, Tocnaye JLB, Djenizian T (2020) High performance stretchable Li-ion microbattery. *Energy Storage Mater* 33:108–115
- Liu QW, Zhang GF, Chen N, Feng X, Wang C, Wang J, Jin X, Qu L (2020) The first flexible dual-ion microbattery demonstrates superior capacity and ultrahigh energy density: small and powerful. *Adv Funct Mater* 30:2002086
- Li WH, Christiansen TL, Li C, Zhou YL, Fei H, Mamakhel A, Iversen BB, Watkins JJ (2018) High-power lithium-ion microbatteries from imprinted 3D electrodes of sub-10 nm $\text{LiMn}_2\text{O}_4/\text{Li}_4\text{Ti}_5\text{O}_{12}$ nanocrystals and a copolymer gel electrolyte. *Nano Energy* 52:431–440
- Salian GD, Lebouin C, Demoulin A, Lepihin MS, Maria S, Galeyeva AK, Kurbatov AP, Djenizian T (2017) Electrodeposition of polymer electrolyte in nanostructured electrodes for enhanced electrochemical performance of thin-film Li-ion microbatteries. *J Power Sources* 340:242–246
- Zhao QN, Zhao KQ, Ji GP, Guo X, Han M, Wen J, Ren Z, Zhao S, Gao Z, Wang R, Li M, Sun K, Hu N, Xu C (2019) High sulfur loading, rGO-linked and polymer binder-free cathodes based on rGO wrapped N, P-codoped mesoporous carbon as sulfur host for Li-S batteries. *Chem Eng J* 361:1043–1052
- Guo QZ, Guo XH, Du KQ et al (2015) Superior high-rate capability of hierarchically structured flower-like magnetite-carbon-graphene composite for Li-ion anode. *Int J Hydrog Energy* 40:1846–1851
- Xue XY, Zhang H, Yuan S, Shi L, Zhao Y, Wang Z, Chen H, Zhu J (2020) PEDOT:PSS @molecular sieve as dual-functional additive to enhance electrochemical performance and stability of Ni-rich NMC lithium-ion batteries. *Energy Technol* 8:2000339
- Lv D, Zheng J, Li Q, Xie X, Ferrara S, Nie Z, Mehdi LB, Browning ND, Zhang JG, Graff GL, Liu J, Xiao J (2015) High energy density lithium-sulfur batteries: challenges of thick sulfur cathodes. *Adv Energy Mater* 5:1402290
- Egorov V, Gulzar U, Zhang Y, Breen S, O'Dwyer C (2020) Evolution of 3D printing method and materials for electrochemical energy storage. *Adv Mater* 32:2000556
- ASTM52900 – 15 (2016) Standard terminology for additive manufacturing general principles – Terminology. ASTM International, West Conshohocken
- Zhang YB, Shi G, Qin JD, Lowe SE, Zhang S, Zhao H, Zhong YL (2019) Recent progress of direct ink writing of electronic components for advanced wearable devices. *ACS Appl Electron Mater* 1:1718–1734
- Sun K, Wei TS, Ahn BY, Seo JY, Dillon SJ, Lewis JA (2013) 3D Printing of interdigitated Li-ion microbattery architectures. *Adv Mater* 25:4539–4543
- Wei TS, Ahn BY, Grotto J, Lewis JA (2018) 3D Printing of customized Li-ion batteries with thick electrodes. *Adv Mater* 30:1703027
- Cao DX, Xing YJ, Tantratian K, Wang X, Ma Y, Mukhopadhyay A, Cheng Z, Zhang Q, Jiao Y, Chen L, Zhu H (2019) 3D printed high-performance lithium metal microbatteries enabled by nanocellulose. *Adv Mater* 31:1807313
- Dai L, Cheng T, Duan C, Zhao W, Zhang W, Zou X, Aspler J, Ni Y (2019) 3D printing using plant-derived cellulose and its derivatives: a review. *Carbohydr Polym* 203:71–86
- Wang QQ, Sun JZ, Yao Q, Ji C, Liu J, Zhu Q (2018) 3D printing with cellulose materials. *Cellulose* 25:4275–4301
- Liu CY, Xu F, Liu YL, Ma J, Liu P, Wang D, Lao C, Chen Z (2019) High mass loading ultrathick porous $\text{Li}_4\text{Ti}_5\text{O}_{12}$ electrodes with improved areal capacity fabricated via low temperature direct writing. *Electrochim Acta* 314:81–88
- Wang Y, Zhu CX, Pfattner R et al (2017) A highly stretchable, transparent, and conductive polymer. *Sci Adv* 3:e1602076
- Rivnay J, Inal S, Collins BA, Sessolo M, Stavrinidou E, Strakosas X, Tassone C, Delongchamp DM, Malliaras GG (2016) Structural control of mixed ionic and electronic transport in conducting polymers. *Nat Commun* 7:11287
- Zhang SM, Chen YH, Liu H et al (2019) Room-temperature-formed PEDOT:PSS hydrogels enable injectable, soft, and healable organic bioelectronics. *Adv Mater* 32:1904752
- Liu Y, Tang DP, Zhong HX, Zhang Q, Yang J, Zhang L (2016) Facial synthesis of nanostructured $\text{Li}_4\text{Ti}_5\text{O}_{12}/\text{PEDOT:PSS}$ composite as anode material for lithium-ion batteries. *RSC Adv* 6:95512–95517

26. Das PR, Komsiyiska L, Osters O, Wittstock G (2015) PEDOT: PSS as a functional binder for cathodes in lithium ion batteries. *J Electrochem Soc* 162:A674–A678
27. Sandu G, Ernould B, Rolland J, Cheminet N, Brassinne J, Das PR, Filinchuk Y, Cheng L, Komsiyiska L, Dubois P, Melinte S, Gohy JF, Lazzaroni R, Vlad A (2017) Mechanochemical synthesis of PEDOT:PSS hydrogels for aqueous formulation of Li-ion battery electrodes. *ACS Appl Mater Interfaces* 9:34865–34874
28. Yuk H, Lu BY, Lin S, Qu K, Xu J, Luo J, Zhao X (2020) 3D printing of conducting polymers. *Nat Commun* 11:1604
29. Naficy S, Jalili R, Aboutaleb SH, Gorkin III RA, Konstantinov K, Innis PC, Spinks GM, Poulin P, Wallace GG (2014) Graphene oxide dispersions: tuning rheology to enable fabrication. *Mater Horiz* 1:326–331
30. Sander JS, Erb RM, Li L et al (2016) High-performance battery electrodes via magnetic templating. *Nat Energy* 1:16099
31. Kuang YD, Chen CJ, Pastel G et al (2018) Conductive cellulose nanofiber enabled thick electrode for compact and flexible energy storage devices. *Adv Energy Mater* 8:1802398
32. Leaf MA, Muthukumar M (2016) Electrostatic effect on the solution structure and dynamics of PEDOT:PSS. *Macromolecules* 49:4286–4294
33. Eliseeva SN, Apraksin RV, Tolstopjatova EG, Kondratiev VV (2017) Electrochemical impedance spectroscopy characterization of LiFePO₄ cathode material with carboxymethylcellulose and poly-3,4- ethylenedioxythiophene/polystyrene sulfonate. *Electrochim Acta* 227:357–366
34. Lama M, Boor SL, Raed H (2016) Carbon nanostructures modified LiFePO₄ cathodes for lithium ion battery applications: optimized porosity and composition. *Mater Res Express* 12:125008
35. Raj H, Rani S, Sil A (2018) Antisite defects in sol-gel-synthesized LiFePO₄ at higher temperature: effect on lithium-ion diffusion. *ChemElectroChem* 5:3525–3532
36. Li Y, Wang J, Fu CC et al (2020) LiFePO₄/C nanoparticle with fast ion/electron transfer capability obtained by adjusting pH values. *J Mater Sci* 56:640–648

Publisher's note Springer Nature remains neutral with regard to jurisdictional claims in published maps and institutional affiliations.